ADVANCED MATERIALS

Supporting Information

for *Adv. Mater.*, DOI 10.1002/adma.202506031

Terahertz Electronic and Spin Currents in Wafer-Scale Van der Waals Bi_2Se_3/WSe_2 Heterostructures and Polymorphs

M. Mičica, A. Wright, S. Massabeau, S. Ayari, E. Rongione, M. Oliveira Ribeiro, S. Husain, R. Sharma, T. Denneulin, R. E. Dunin-Borkowski, J. Mangeney, J. Tignon, R. Lebrun, H. Okuno, O. Boulle, A. Marty, F. Bonell, F. Carosella, H. Jaffrés, R. Ferreira, J.-M. George, M. Jamet and S. Dhillon**

Supplementary Information : Terahertz Electronic and Spin currents in Wafer-Scale Van der Waals $\mathbf{Bi_2Se_3/WSe_2}$ Heterostructures and Polymorphs

M. Mičica,[1], A. Wright,[1], S. Massabeau,[2] S. Ayari,[3,1] E. Rongione,[1,2], M. Oliveira Ribeiro[4] S. Husain, [2] R. Sharma,[4] T. Denneulin,[4] R. Dunin-Borkowsk,[4] J. Tignon,[1] J.Mangeney ,[1] R. Lebrun,[2] H. Okuno,[6] O. Boulle,[4] A. Marty,[4], F. Bonell, [4] F. Carosella [1], H. Jaffres, [2] R. Ferreira,[1] J-M. George,[2] M. Jamet [4], and S. Dhillon,[1]

[1] *Laboratoire de physique de l'Ecole Normale Supérieure, (LPENS), ENS, Université PSL, CNRS, Sorbonne Université, Université Paris Cité, 75005, Paris, France*

[2] *Laboratoire Albert Fert, CNRS, Thales, Université Paris-Saclay, 91767 Palaiseau, France*

[3] *De Vinci Higher Education, Research Center, 92916 Paris La Défense, France*

[4] *Univ. Grenoble Alpes, CEA, CNRS, Grenoble INP, IRIG-SPINTEC, F-38000 Grenoble, France*

[5] *Ernst Ruska-Centre for Microscopy and Spectroscopy with Electrons, Forschungszentrum Jülich, D-52425 Jülich, German*

[6] *Univ. Grenoble Alpes, CEA, IRIG-MEM, 38000 Grenoble, France*

Corresponding authors: matthieu.jamet@cea.fr; sukhdeep.dhillon@phys.ens.fr

I. GROWTH AND STRUCTURAL CHARACTERISATION

Epitaxial growth of $Bi_2Se_3/WSe_2/Co$ heterostructures was perfomed in Spintec facilities. All the Bi_2Se_3(10QL)/WSe_2(t_{TMD})/Co(3nm) heterostructures were grown by molecular beam epitaxy (MBE) on large area sapphire substrates (cm^2) under ultra high vacuum (UHV) with a base pressure in the low 10^{-10} mbar range. Sapphire substrates were annealed during 30 minutes at 300°C and one hour at 1000°C in air before being introduced in the MBE reactor to promote the formation of a terrace-and-step smooth surface. The substrate was further annealed at 700°C during 30 minutes under UHV prior to the growth. 10 quintuple layers (QL) of Bi_2Se_3 and 1-4 monolayers (ML) of WSe_2 were then epitaxially grown on sapphire at 270°C. Bismuth and tungsten were evaporated using an electron gun at 0.075 Å/s and 0.00625 Å/s rates, respectively. Selenium was co-evaporated using a standard Knudsen cell with a partial pressure of 1.2×10^{-6} mbar measured at the sample position. The stack was then annealed at 550° during 5 minutes to improve the crystal quality. 3 nm of cobalt and aluminum were then evaporated on top at room temperature at 0.1 Å/s and 0.5 Å/s rates, respectively.

In Figure S1, we investigated the stacking of WSe_2 layers by STEM. In flat areas (Figure S1(a), WSe_2 grows up to 2 ML with the 2H stacking order (opposite chevrons) whereas 3R stacking (parallel chevrons) starts to form for thicker films. Moreover, at Bi_2Se_3 step edges (Fig. S1(b), we found the formation of defects with mixed 2H and 3R stacking.

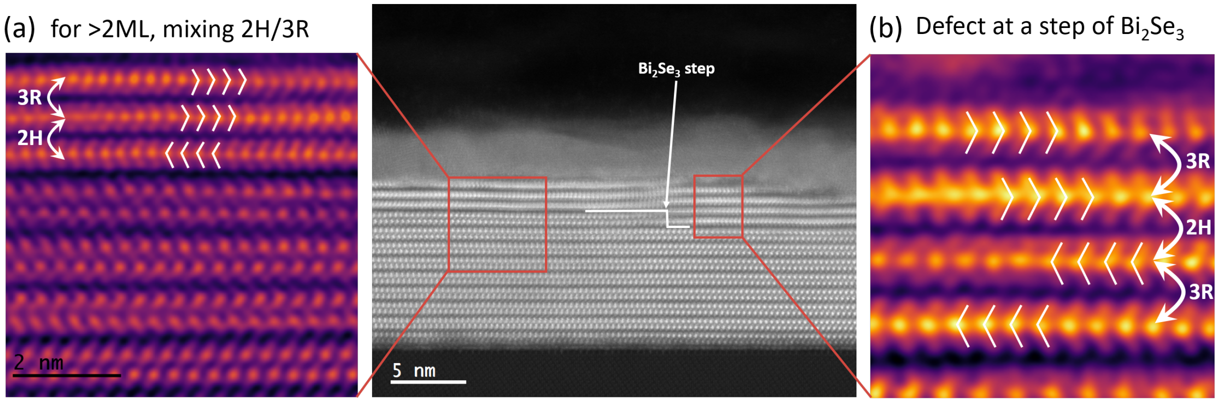

Figure S1: Atomic scale atomic images of Bi_2Se_3(10QL)/WSe_2(4ML)/Co(3nm)/Al(3nm) showing WSe_2 stacking sequence on (a) a flat area of Bi_2Se_3 and (b) at a Bi_2Se_3 step edge.

.

II. RAMAN SPECTROSCOPY

In order to confirm the monolayer nature and thickness of the deposited WSe_2 spacer, we performed Raman spectroscopy with an excitation wavelength on the $Bi_2Se_3/WSe_2/Co$ stacks as a function of WSe_2 thickness as shown in Figure S2. Raman peaks characterization is conducted with a excitation laser of central wavelength of 532 nm.

We observe in Figure S2(a) for 3 ML WSe_2 that the Raman response is dominated by A^1_{1g}, A^2_{1g} and E_{2g} modes at 72 cm^{-1}, 174 cm^{-1} and 130 cm^{-1}, respectively, corresponding to previous observations [1]. An additional fourth peak around 250 cm^{-1} is measured only in samples with WSe_2 and corresponds to the WSe_2 Raman modes. The Raman spectrum as a function of WSe_2 thickness is presented in Figure S2(b), showing how the Raman peak amplitude as well as the peak shape varies with the WSe_2 thickness. The deconvolution of the each Raman modes is presented in Figures S2(c-e) for each structure using three Gaussian fits. The extracted WSe_2 Raman modes are presented in Figure S2(f) as a function of WSe_2 thickness. The evolution of the A_{1g}, E_{1g} and $2LA$ peaks' Raman shifts are in close agreement with the literature on WSe_2 layers [2], thus confirming the deposited thickness by MBE. Note that the different phases of WSe_2 have similar Raman modes, increasing the width of the Raman peaks.

The uniformity of the MBE grown were investigated at microscopic and macroscopic areas to highlight the uniformity of the MBE grown samples. Here, we investigated Bi_2Se_3(10QL)/WSe_2(2ML) structures. Figure S3 shows the Raman intensity map of the heterostructure at micrometer scales, highlighting the uniformity of the MBE grown structure. Figure S4 shows the uniformity at macroscales where the Raman spectrum is taken at a range of macroscopic positions over the grown sample.

III. THZ EMISSION SPECTROSCOPY

A. THz experimental setup

A custom THz TDS setup was used to measure the ultrafast photocurrents from the generated THz pulses. An ytterbium amplifier coupled OPA system in transmission configuration where linearly polarized 51 mW pump pulse (OPA set at 780 nm, ≈80 fs, 150 kHz, ≈1 mm spot diameter) excites the front surface of the samples and THz pulse is collected

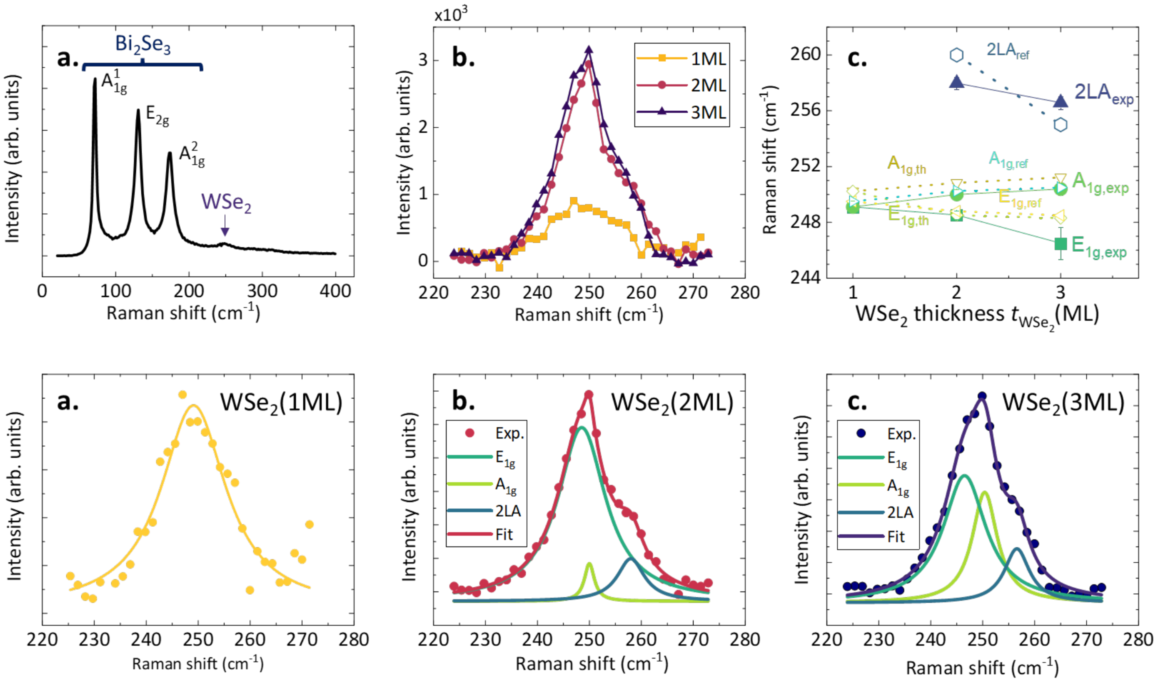

Figure S2: **Raman spectroscopy of trilayers while varying the $\mathbf{WSe_2}$ spacer.** (a) Raman response of Bi_2Se_3(10QL)/WSe_2(3ML)/AlO_x(3) with the strong Raman peaks from Bi_2Se_3 and weaker peak from WSe_2 around 250 cm^{-1}. (b) Relative intensity of the WSe_2 Raman peak as a function of t_{TMD} ranging from 1 to 3 ML. (c-e) Deconvolution of the Raman peaks respectively for 1, 2 and 3 ML of WSe_2. (f) Evolution of the extracted A_{1g}, E_{1g} and $2LA$ peak intensities as a function of WSe_2 thickness. The data are compared to Ref. [2] (dotted lines). Error bars correspond to standard deviations.

from the back. Here the pump power was kept at 51 mW to avoid damage to the sample or saturation effects. In this regime the generated field is expected to be linear with pump fluence. The samples were place in rotating stage to allowing in-plane rotation (angle ϕ) between fixed poles of electromagnet providing 20 mT strong magnetic field. THz pulses were acquired by standard electro-optic sampling with sampling pulse from main oscillator (1030 nm, 150 fs, 150 kHz) and 500 µm-thick [110] ZnTe crystal. The pump beam was modulated by optical chopper at ≈946 Hz and measurement compartment was purged by dry nitrogen gas.

B. Polarity determination of THz time domain pulses

The polarity (i.e. the postive or negative sign of the generated THz pulse) of the acquired signals was automatically processed by software. As pulses can differ in their shape two

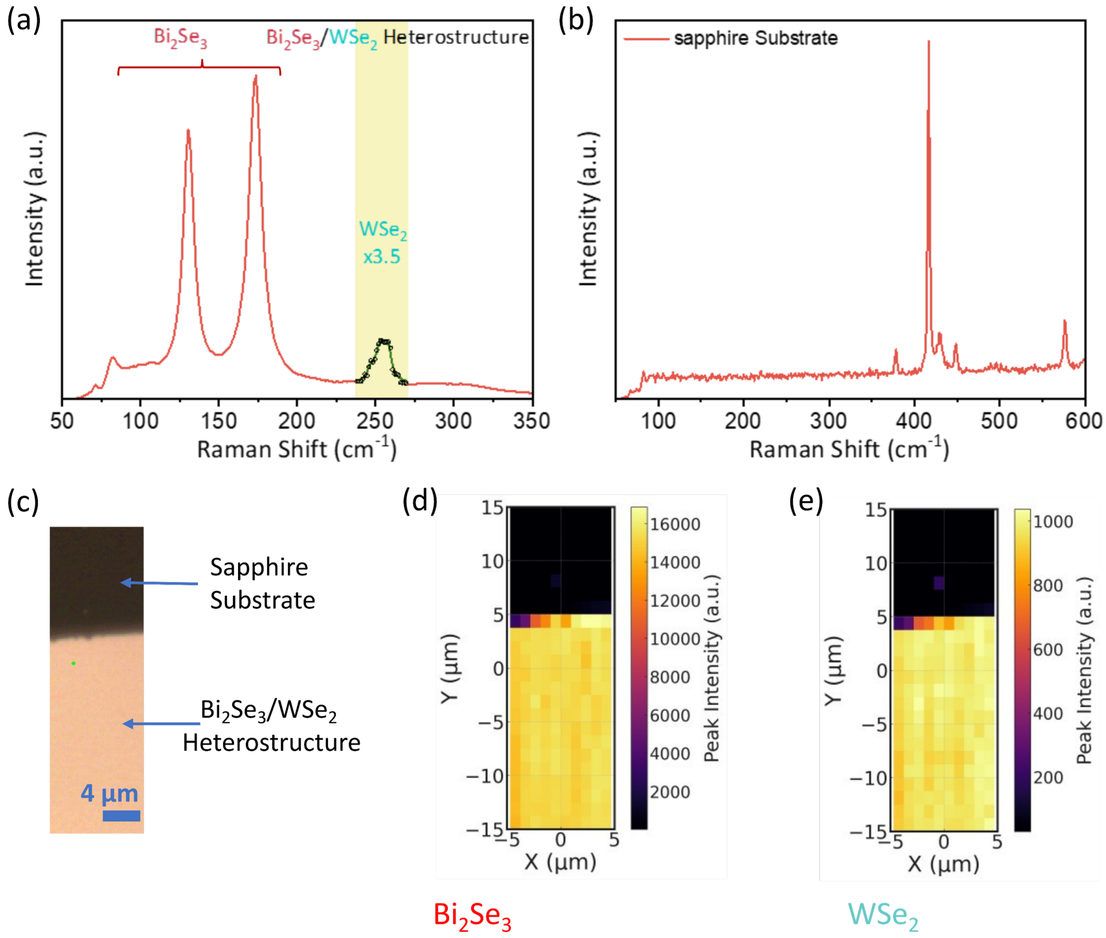

Figure S3: **Raman microscopy of heterostructures with WSe_2 (2ML) layer.**(a) Typical Raman spectrum of Bi_2Se_3(10QL)/WSe_2($2ML$) on sapphire sample showing characteristic vibration modes of Bi_2Se_3(in red) and the Raman peak of WSe_2 (in green) that corresponds to a convolution of the various Raman modes of WSe_2. The WSe_2 peak intensity is multiplied by 3.5 and a baseline is then subtracted for better visibility. (b) Raman spectrum of the pristine sapphire substrate. (c) Optical image of the sample exhibiting both pristine sapphire substrate and the Bi_2Se_3/WSe_2 film. (d-e) $10{\times}30$ μm^2 Raman intensity maps of $Bi_2Se_3$and WSe_2 Raman peaks showing the very good homogeneity over microscopic scales of the MBE grown sample. The Raman Spectra and Raman mapping is done using a 633 nm laser.

methods were applied:

I) Polarity was determined by comparing absolute values of minima and maxima in time domain signals, i.e. if the absolute value of the maximum is higher then the pulse is positive, otherwise it is negative

II) Polarity was determined by comparing position of minima and maxima in time, i.e. if the position of minimum is before the position of maximum the pulse is positive, otherwise it is negative.

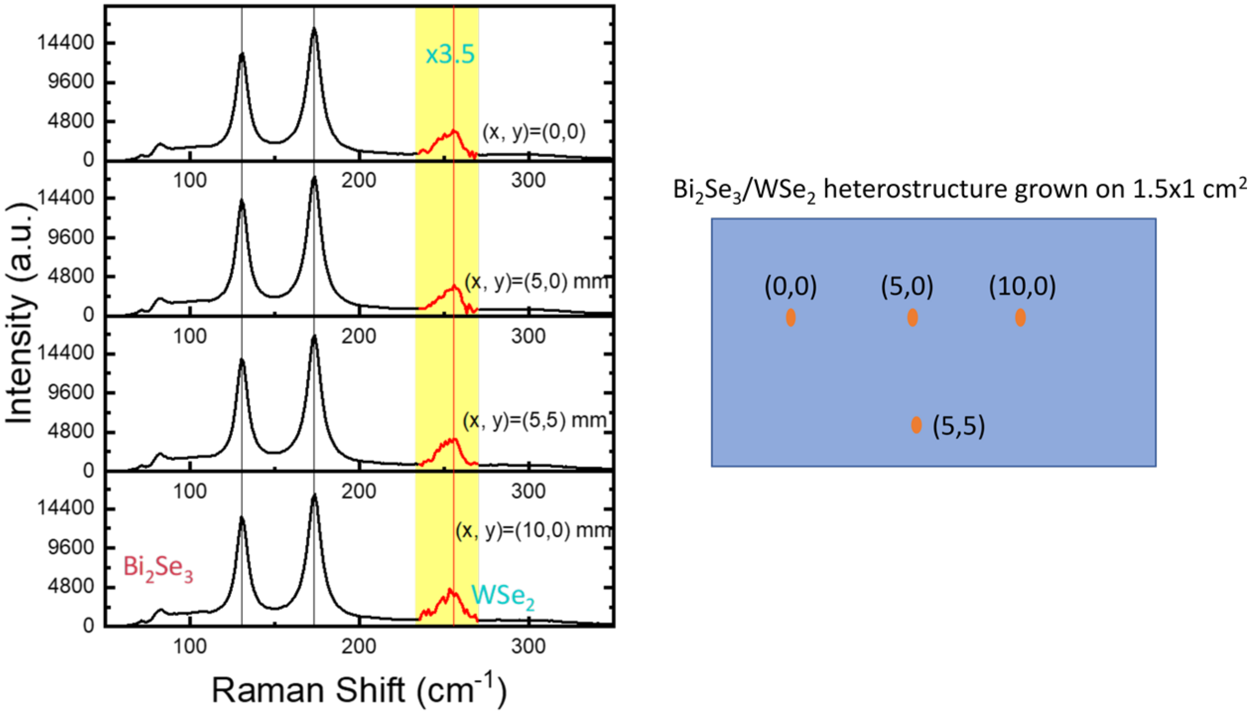

Figure S4: **Raman spectra over sample surface.** Raman spectra recorded at different positions on the sample demonstrating the large-scale macroscopic homogeneity of the film. The WSe$_2$ peak intensity is multiplied by 3.5 and a baseline is then subtracted for visibility.

Results obtained by this two methods can slightly wary depending on the symmetry of pulses as shown in Figure S5. The first (I) method perform well for symmetric pulses (Figure S5(a)) where is a distinct difference between absolute values of maxima and minima. For asymmetric pulses (Figure S5(b)), where absolute values of maxima and minima are comparable, the second method (II) yields better (more continuous) results as even the small noise can flip the polarity when using the first method.

Sample Bi$_2$Se$_3$/WSe$_2$(#)/Co	0 ML	1 ML	2 ML	3 ML	4 ML
Method	I/II*	I	II	I	I*/II

Table SI: Applicable methods for assignment of THz pulse polarity. For samples with 0 and 4 ML WSe$_2$, both methods are usable (methods with (*) were used for these samples)

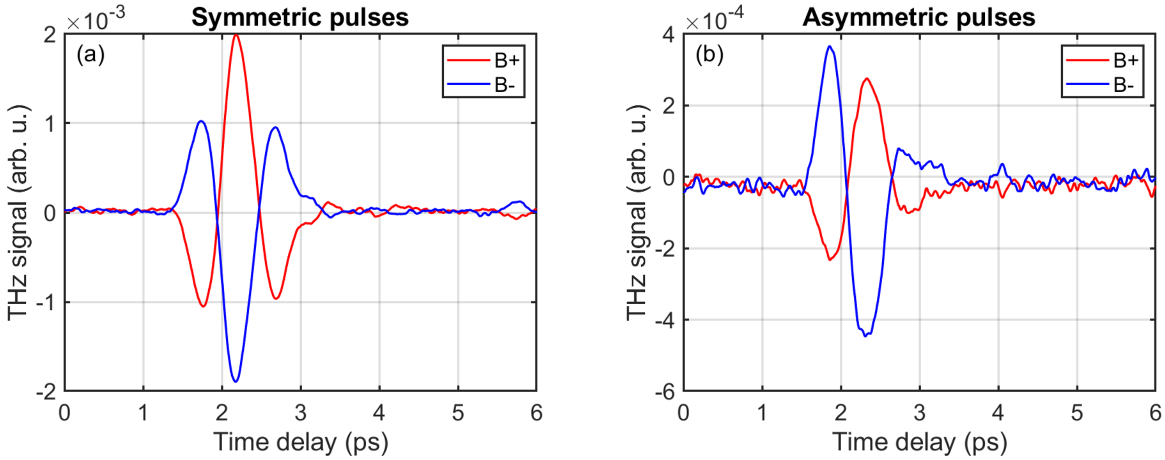

Figure S5: Time domain THz pulses with different symmetry. (a) symmetric pulse - polarity can be easily determined by comparing absolute values of minima and maxima. (b) asymmetric pulses with comparable absolute values of minima and maxima, where polarity depend on their position in time.

IV. COMPUTATIONAL METHODS

A. Ground-state calculations from first-principles.

Structural relaxation and electronic band structure properties of ML and 2 ML WSe_2 with various polytypic structures (2H, 3R, and 1T$'$) were investigated using Density Functional Theory (DFT). The calculations were carried out with the Quantum ESPRESSO (QE) simulation package, with full-relativistic norm-conserving pseudopotentials in order to take into account spin orbit coupling (SOC) and exchange-correlation functional in the Perdew-Berke-Ernzerhof's form (PBE) within the generalized-gradient approximation (GGA) [3–6]. Since WSe_2 has a layered structure, the van der Waals (vdW) force between different layers are taken into account by first-principles calculations for a better accuracy [7–11]. In our work, since, GGA+PBE methods do not describe the long-range coulomb interaction, a vdW correction of the PBE functional is therefore performed using the empirical correction scheme of Grimme (DFT + D/PBE)[7, 10, 11]. This approach has been successful in describing layered structures [12–14]. To ensure numerical stability, a convergence study using PBE-GGA calculations was conducted, testing the cutoff energy and k-point sampling to achieve total energy convergence. The kinetic energy cutoff for a plane-wave basis set was taken as 680 eV. The Monkhorst- Pack k-point sampling of $20 \times 20 \times 1$, and $40 \times 40 \times 1$ was adopted for the Brillouin zone (BZ) integration, to achieve converged results for the calculation of structural relaxation and electronic structures, respectively. The initial lattice constant for bulk WSe_2 is taken from the materials project website [15], and is optimized for the chosen pseudo-potential, by using the quasi-Newton schemes as implemented in the QE package [16]. The optimized lattice constants of the bulk are then used as initial parameters for the 1 ML and 2 ML then relaxed. A large vacuum region of 30 Å was applied to the plane normal direction to minimize image interactions from the periodic boundary condition. The convergence criterion of self-consistent calculations for electronic structure and ionic relaxations is to reach a 10^{-8} eV difference between two consecutive steps. During the optimization process, all atoms were free to move in all directions of space to minimize the internal forces down to 10^{-5} Rydbergs per Bohr radius.

Second harmonic generation (SHG) was calculated using the independent particle approximation (IPA) as implimented in YAMBO code, (see ref [17–22]). Convergence was obtained using a $20 \times 20 \times 1$k-point grid for 1H and 3R WSe_2, and $15 \times 15 \times 1$ for 1T′ WSe_2. We have considered 50 bands in our calculation. A time step of 0.0025 fs was used to guarantee accuracy and stable results. We add a dephasing term with 6 fs to simulate a finite broadening of about 0.2 eV, and propagate for 55 fs for each laser frequency.

Beside the dimensionality, stacking orders and symmetry significantly affect the electronic and optical properties of layered TMD materials. In fact, the arrangement of chalcogen atoms and the stacking sequence of layers result in a variety of polytypic structures, such as 2H, 3R, 1T, and 1T′, each exhibiting distinct properties [23–29]. In this section, we will focus on how these stacking configurations and atomic arrangements influence the electronic and nonlinear (SHG) optical properties in ML and 2 ML WSe_2. 1 ML form of the H phase, termed the 1H phase, is built on a hexagonal crystal system and follows a trigonal lattice arrangement. In this configuration, Se atoms form a hexagonal close-packed structure, while W atoms are positioned between two atomic layers of Se atoms, creating a trigonal prismatic geometry with Bernal (ABA) stacking. The H phase can have varied polytypes due to different stacking sequence of layers [23, 29–31]. The 2H phase, which is the most common one, adds a screw rotation in the symmetry resulting from the AB stacking of the second layer while maintaining the hexagonal crystal system [23, 29, 30, 32, 33]. The 3R phase reduces the rotation symmetry from 6-fold to 3-fold resulting in a rhombohedral lattice, with an ABC stacking sequence, which alters both electronic and optical properties [25, 30]. The T phase, found in both 1 ML and multilayer forms, adopts an AA stacking sequence, with W atoms arranged in an octahedral coordination surrounded by Se atoms

[29, 31, 33, 34]. It has been known that the 1T structure in TMD is typically unstable in free-standing condition, leading to a spontaneous lattice distortion along the x direction. This distortion results in a period configuration, known as the 1T′ structure. In this latter, the originally ordered octahedral coordination becomes disordered, creating distinctive one-dimensional zigzag chains along the y direction [23, 35]. The 1H and 1T phases of WSe_2 are hexagonal, with optimized lattice parameters of 3.19 Å and 3.17 Å, respectively. In contrast, the unit cell of 1T′ WSe_2 is rectangular, with optimized lattice parameters of $a = 5.944$ Å and $b = 3.301$ Å [25, 34–36]. In the 2 ML configuration, the in-plane lattice parameters remain nearly identical to those of the 1 ML structure ($a = 3.2$ Å, 3.175 Å and 5.98 Å for 2H, 1T and 1T′, respectively). This feature arises from the strong covalent bonding between W and Se atoms within each layer. Notably, the weak van der Waals interactions between adjacent layers exert minimal influence on the intrinsic in-plane bonding, which lead to preserving the in-plane lattice parameters of individual layers [12–14, 37].

The band structures of 1H, 1T, and 1T′ phases for the 1 ML WSe_2 and the 2H, 3R, 1T, and 1T′ phases for the 2 ML configuration are shown in Figures S6 and S7, respectively. We can clearly notice that the electronic properties of TMDs show a significant dependence on the polytypic structures. For H phase, going from 1 ML to 2 ML, WSe_2 exhibit a transition from a direct to an indirect band gap with an energy of 1.3 eV (Figures S6 a and S7 a). The valence band maximum (VBM) is located at the Γ point, while the conduction band minimum (CBM) is positioned midway between the Γ and K points. This results are consistent with previous DFT calculations in GGA approximation [38, 39]. Similar to 2H phase, 3R has an indirect band gap of 1.2 eV. However, in contrast to the H phase, 3R maintains the broken inversion symmetry from ML to bulk. The impact of the lack of inversion symmetry can be clearly seen in the conduction and valence band splitting in the 3R band structure, which is not present in the 2H bands (Figures S7 b). This splitting is due to the different atomic environments of the tungsten atoms in each layer of a 3R-stacked bilayer [40]. In contrast to 2H and 3R phases the 1T-WSe_2 phases show a metallic character for 1 and 2 ML (Figure S7c and S6c). 1 ML WSe_2 in the 1T′ phases is a semiconductor with a bandgap of about 0.08 eV [23, 35, 41]. The CB and VB display a camelback shape near Γ in the 2D Brillouin zone (BZ) (see Figure S6b) suggestive of band inversion. Notably, in the absence of SOC, this band inversion leads to the appearance of two Dirac cones centered at finite momenta on $Y - \Gamma - Y$ in 2D BZ [23, 35]. In the 2 ML, the interlayer electronic

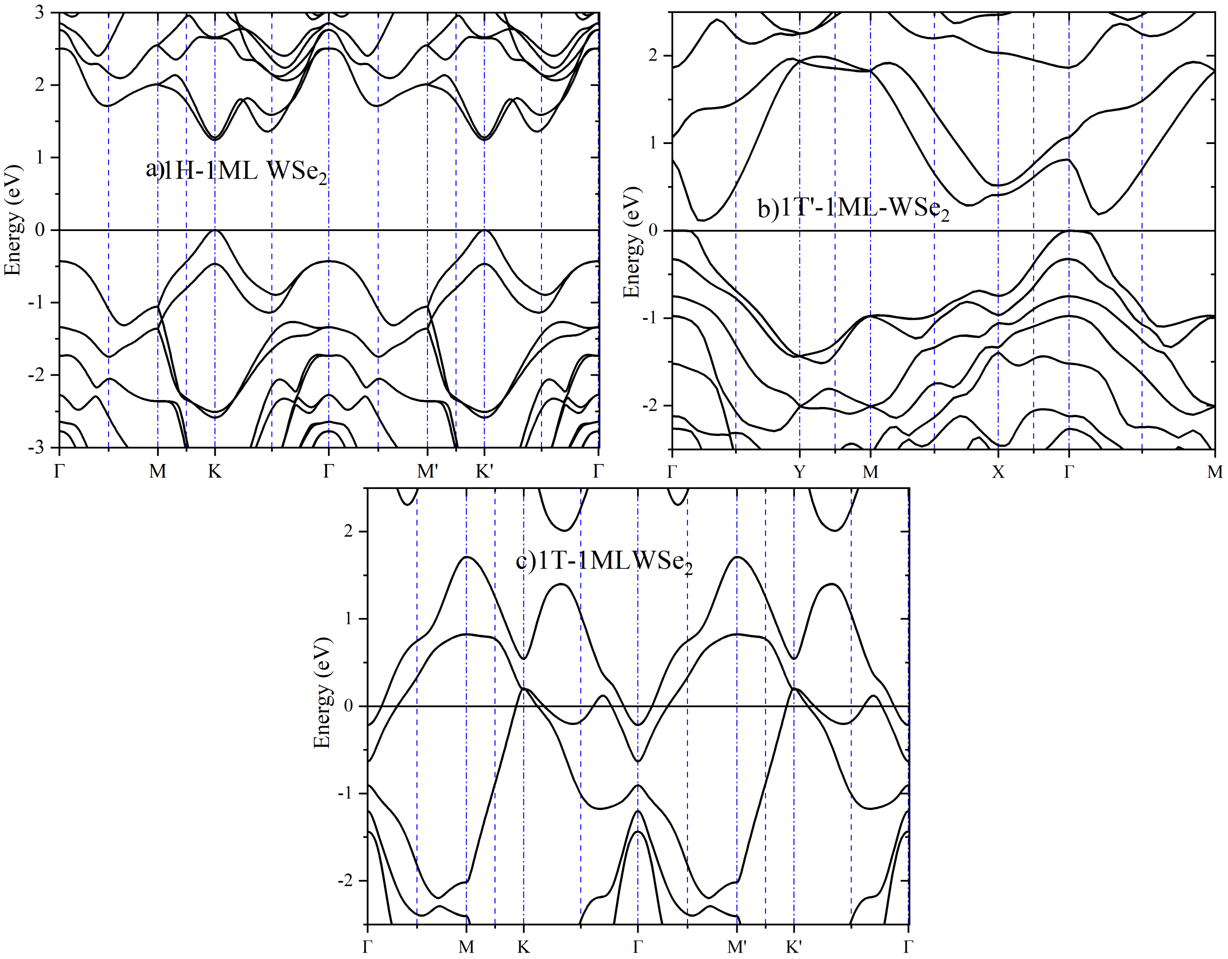

Figure S6: Electronic band structure for (a) 1H, (b) 1T′ and (c) 1T 1 ML WSe$_2$

hybridization increases leading to a semiconductor-to-semimetal transition (Figure S7 b).

The nonlinear optical (NLO) frequency conversion efficiency of 2D layered crystals is highly sensitive to their lattice symmetry and thickness. In Figures S8, S9 and S10, we calculate the SHG for stacking configurations that exhibit non-zero second-order nonlinear properties. Notably, in the 2H phase of WSe$_2$, the symmetry is different for odd and even number of layers. For even-layered structures, the symmetry point group is D_{3d} ($\bar{3}m$). In this case, the natural Bernal stacking order quenches the SHG owing to its centrosymmetric symmetry. Qualitatively, this is because the constituent monolayers in the bilayer are rotated by an angle of π with respect to each other in 2H stacking, and the electric field at a double frequency generated in one layer is compensated by the contribution of the other. In contrast, odd-layered structures adopt the non-centrosymmetric D_{3h} ($\bar{6}m2$) point group, which lacks an inversion center and thereby can induce second-order NLO frequency conversion [42, 43].

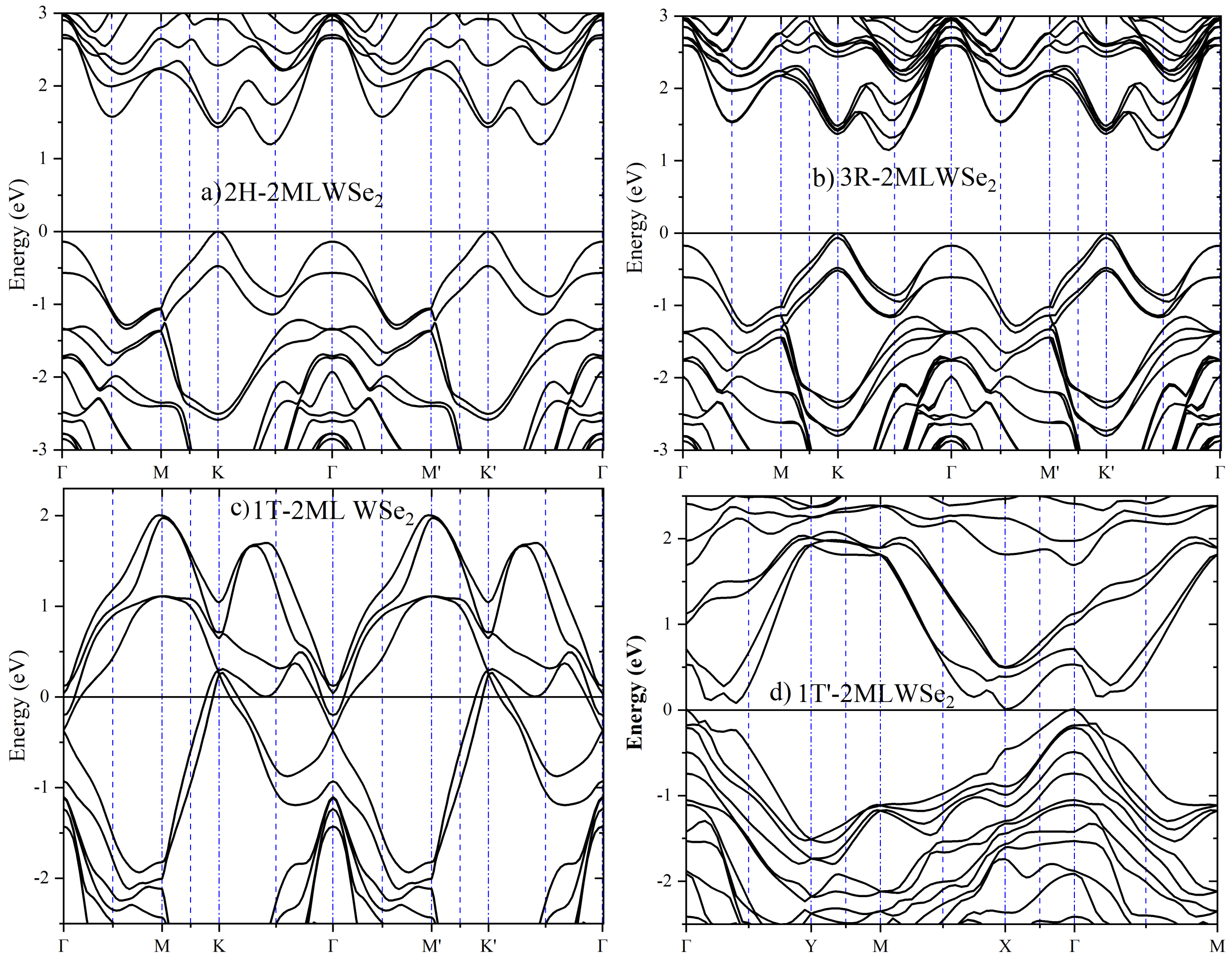

Figure S7: Electronic band structure for (a) 2H, (b) 3R and (c) 1T (d) 1T′ 2 ML WSe$_2$

In Fig. S8, we show the xxy component of SHG susceptibility tensors computed using IPA approximation as implemented in yambo code [17–22]. In general, χ^2_{ijk} as a tensor in 2D has 8 components; however, for our system with D_{3h} symmetry, the χ^2 tensor exhibits four nonzero elements, namely $\chi^2_{yyy} = -\chi^2_{yxx} = -\chi^2_{xxy} = -\chi^2_{xyx}$, where x, y, z denote the crystalline coordinates [44]. Here, x-axis is defined along the armchair direction of the hexagonal plane, which is 30° from the zigzag direction.

Compared to the 2H phase, 3R WSe$_2$ has the polar point group symmetry of C_{3v} ($R3m$), in which the adjacent layers displace slightly from each other without any rotation. This phase maintains broken inversion symmetry from ML to bulk, and induces high-frequency conversion efficiency compared to 2H bulk counterpart whish could serve as an appropriate candidate for the research of nonlinear optics. In figure S9, we display the real and imaginary parts of χ^2_{xxy} as well as the absolute value of the SHG susceptibility. As compared to the

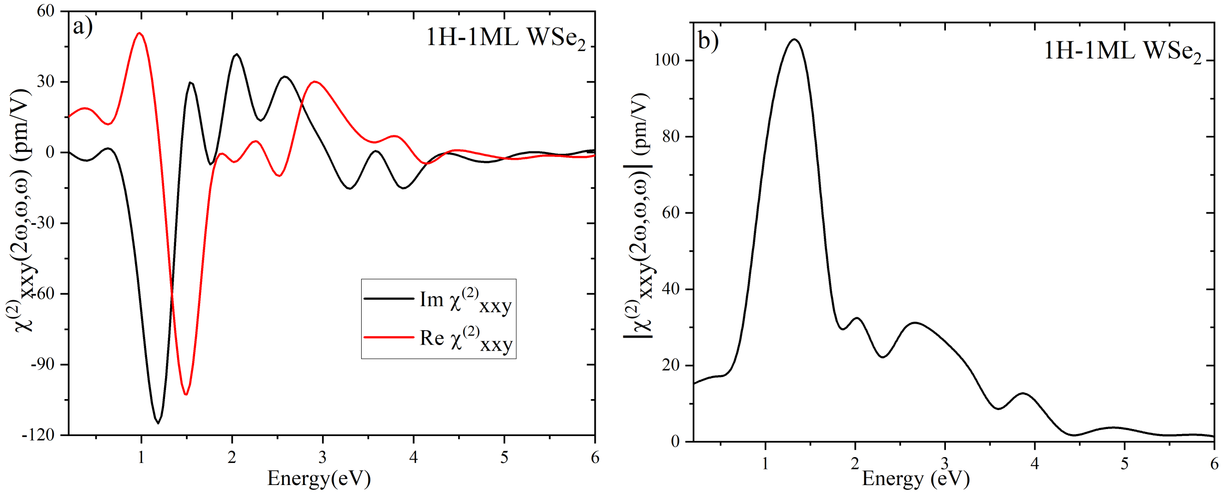

Figure S8: Calculated real and imaginary parts (a) and absolute value (b) of the SHG susceptibilities in 1H 1 ML-WSe$_2$

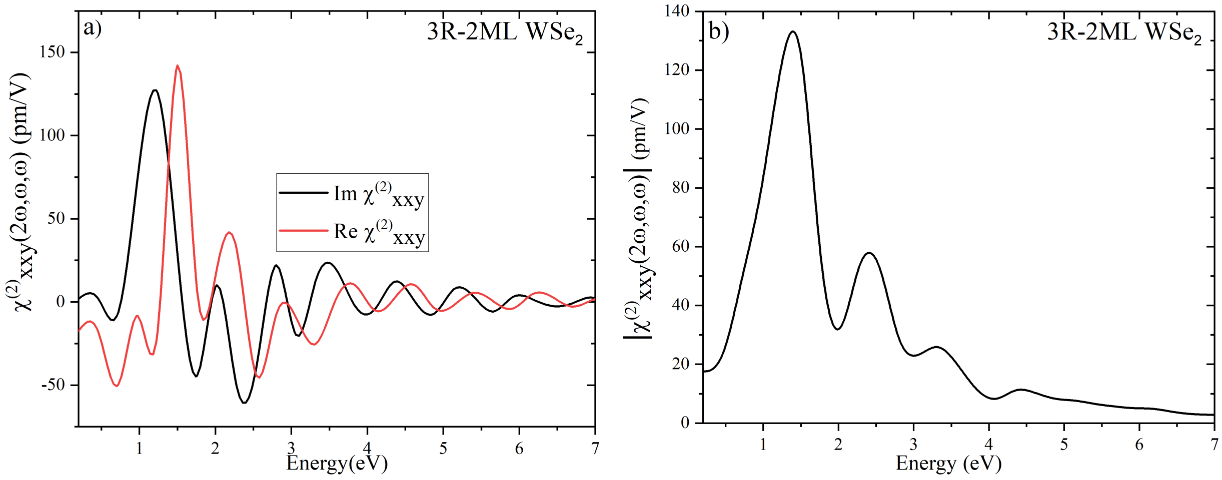

Figure S9: Calculated real and imaginary parts (a) and absolute value (b) of the SHG susceptibilities in 3R 2 ML-WSe$_2$

1H 1 ML WSe$_2$, 3R 2 ML WSe$_2$ shows stronger SHG intensity and more complex resonance behavior, reflecting the influence of bilayer stacking and interlayer coupling on the electronic and nonlinear optical properties [45, 46].

Figure S11 (a,b) illustrates polarization-dependent SHG intensities of 1H phase as well as 3R phase WSe$_2$. We found that the SHG polarization depicts a typical six-fold rotational symmetry corresponding to three-fold rotational symmetry of WSe$_2$, and show a six-petal pattern, which is consistent with the previous studies and well confirmed in our experiments.

The 1T phase, both in ML and multilayer forms belongs to the D_{3d} space group, with an inversion centers are at W sites. The symmetry of 1T does not support SHG due to the presence of inversion symmetry, thus limiting its effectiveness in nonlinear optical applica-

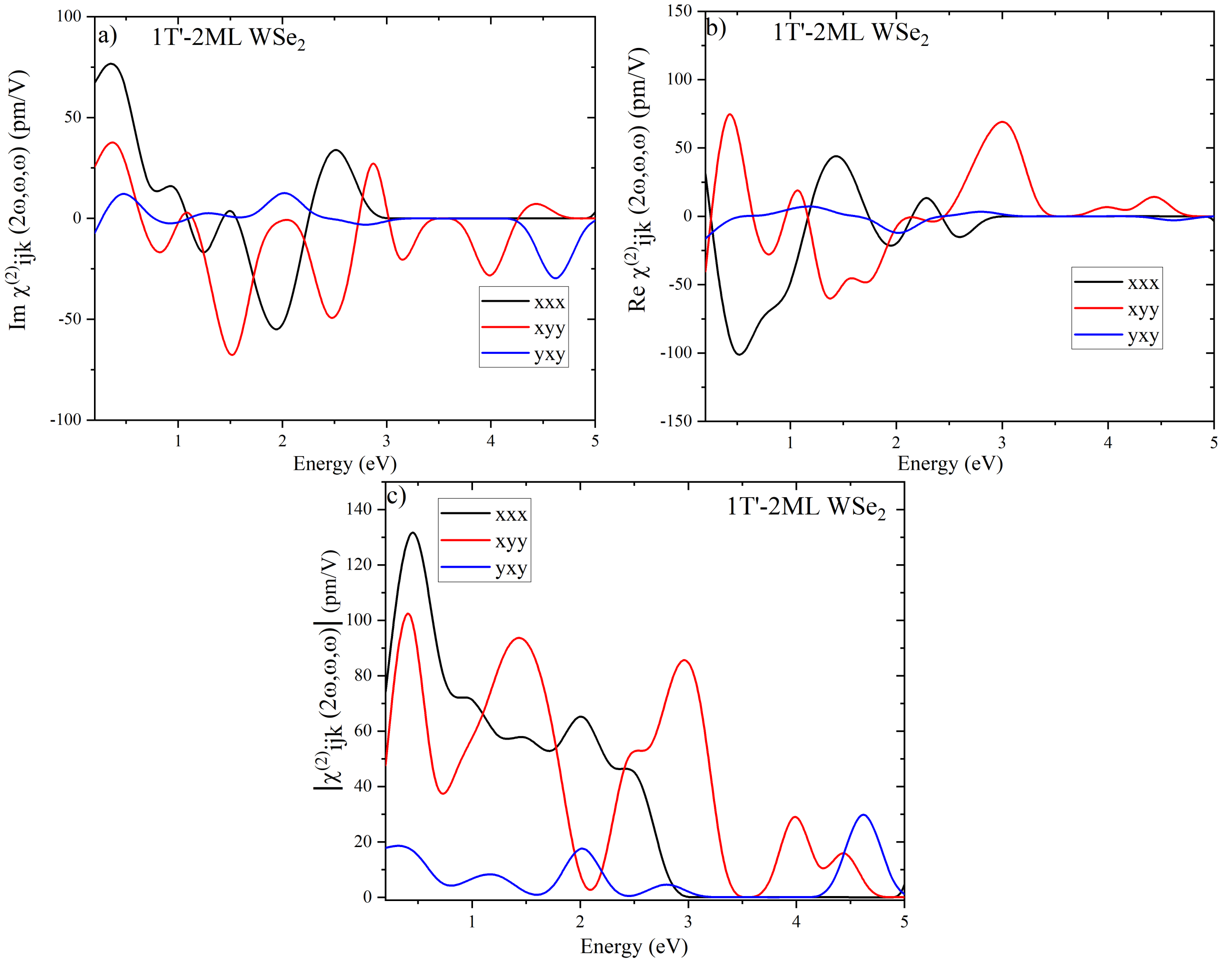

Figure S10: Calculated imaginary parts (a) , real part (b) and absolute value (c) of the SHG susceptibilities in $1T^{'}$ 2 ML-WSe$_2$

tions. However, bulk 1T′ WSe$_2$ is a centrosymmetric materials belonging to the space group C_{2h}^2 ($P2_1/m$). The same symmetry is preserved in samples with an odd number of layers, including monolayer. However, the inversion symmetry is broken for even number of layers of 1T′ WSe$_2$, and the crystal structure falls into the C_s^1 (Pm) space group. This breaking of symmetry leads to a significant second order non linear effect.

In Figure S10, we plot the real, imaginary, and absolute values of the SHG response in the 1T′ phase of 2 ML WSe$_2$. Compared to the 1H and 3R phases, the 1T′ phase exhibits multiple sharp resonances with magnitudes comparable with the other phase. Unlike the relatively smooth SHG peaks of the 1H and 3R phases, the real and imaginary parts in the 1T′ phase oscillate dramatically, reflecting its fundamentally different electronic structure and symmetry. Furthermore, unlike the 1H and 3R phases, which have simpler and more isotropic SHG responses, the 1T′ phase shows distinct tensor components (χ^2_{xxx}, χ^2_{xyx}, χ^2_{yxy})

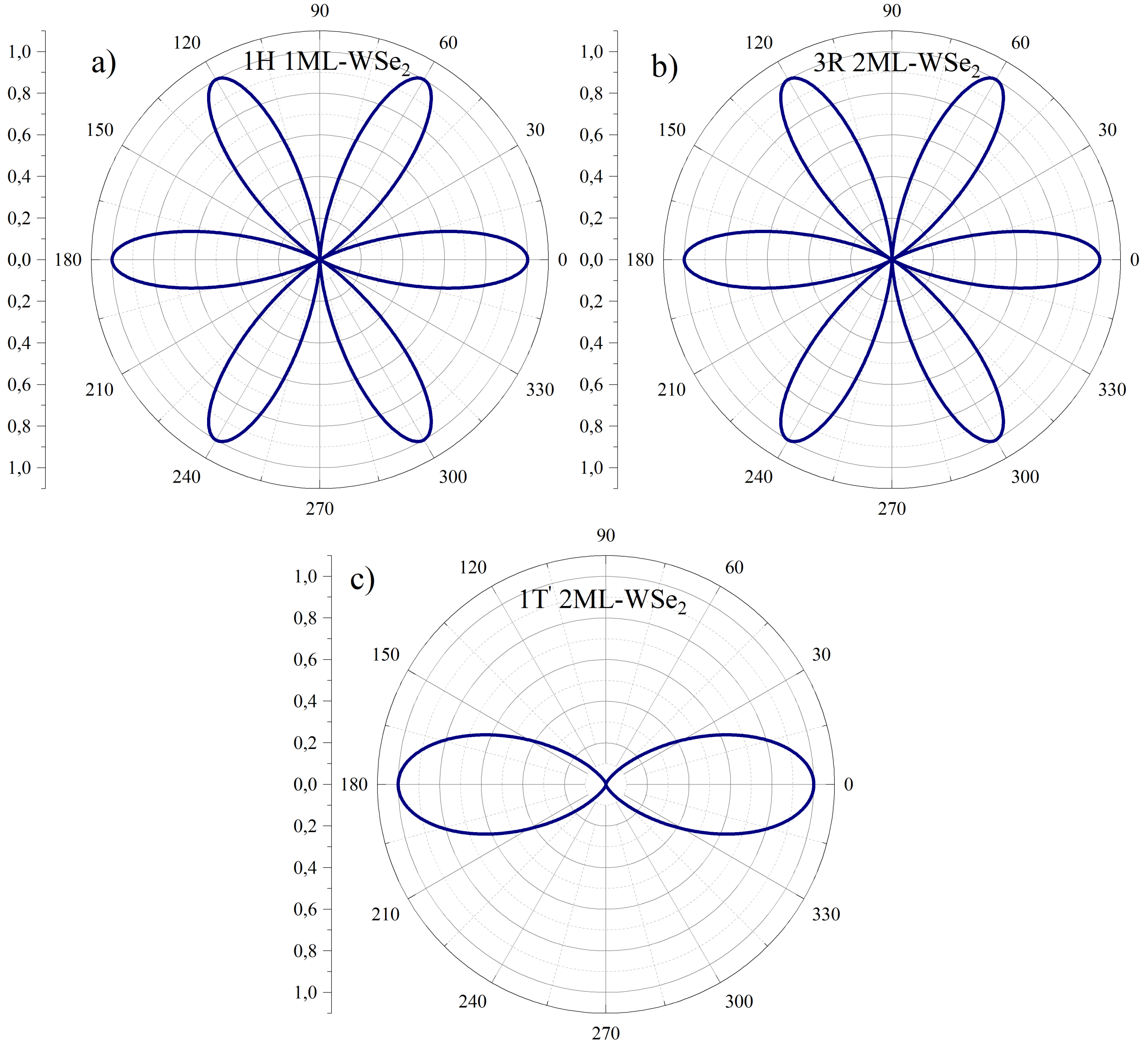

Figure S11: The polarization-resolved SHG for the 1H-1 ML WSe$_2$ (a), 3R (b) and 1T′ (c) -2 ML WSe$_2$ phase (Polar plots)

with vastly different phase relationships. In Figure S11, we present the polarization-resolved SHG for the 1T′ phase, revealing a two-petal pattern. This behavior arises from structural distortion, which reduces the symmetry from threefold to twofold, aligning well with our experimental results.

[1] J. Zhang, Z. Peng, A. Soni, Y. Zhao, Y. Xiong, B. Peng, J. Wang, M. S. Dresselhaus, and Q. Xiong, Raman Spectroscopy of Few-Quintuple Layer Topological Insulator Bi$_2$Se$_3$ Nanoplatelets, Nano Letters **11**, 2407 (2011), pMID: 21604748.

[2] W. Zhao, Z. Ghorannevis, K. K. Amara, J. R. Pang, M. Toh, X. Zhang, C. Kloc, P. H. Tan, and G. Eda, Lattice dynamics in mono- and few-layer sheets of WS_2 and WSe_2, Nanoscale **5**, 9677 (2013).

[3] P. Giannozzi, S. Baroni, N. Bonini, M. Calandra, R. Car, C. Cavazzoni, D. Ceresoli, G. L. Chiarotti, M. Cococcioni, I. Dabo, et al., Quantum espresso: a modular and open-source software project for quantum simulations of materials, Journal of physics: Condensed matter **21**, 395502 (2009).

[4] P. Giannozzi, O. Andreussi, T. Brumme, O. Bunau, M. B. Nardelli, M. Calandra, R. Car, C. Cavazzoni, D. Ceresoli, M. Cococcioni, et al., Advanced capabilities for materials modelling with quantum espresso, Journal of physics: Condensed matter **29**, 465901 (2017).

[5] J. P. Perdew, K. Burke, and M. Ernzerhof, Generalized gradient approximation made simple, Physical review letters **77**, 3865 (1996).

[6] R. Sabatini, E. Küçükbenli, C. H. Pham, and S. de Gironcoli, Phonons in nonlocal van der waals density functional theory, Physical Review B **93**, 235120 (2016).

[7] S. Grimme, Accurate description of van der Waals complexes by density functional theory including empirical corrections, Journal of computational chemistry **25**, 1463 (2004).

[8] M. Dion, H. Rydberg, E. Schröder, D. C. Langreth, and B. I. Lundqvist, Van der Waals density functional for general geometries, Physical review letters **92**, 246401 (2004).

[9] R. Sabatini, T. Gorni, and S. De Gironcoli, Nonlocal van der Waals density functional made simple and efficient, Physical Review B **87**, 041108 (2013).

[10] Q. Wu and W. Yang, Empirical correction to density functional theory for van der Waals interactions, The Journal of chemical physics **116**, 515 (2002).

[11] S. Grimme, J. Antony, S. Ehrlich, and H. Krieg, A consistent and accurate ab initio parametrization of density functional dispersion correction (DFT-D) for the 94 elements H-Pu, The Journal of chemical physics **132**, 10.1063/1.3382344 (2010).

[12] X. Fan, W. Zheng, J.-L. Kuo, D. J. Singh, C. Q. Sun, and W. Zhu, Modulation of electronic properties from stacking orders and spin-orbit coupling for 3R-type MoS_2, Scientific reports **6**, 24140 (2016).

[13] G. Mercurio, E. R. McNellis, I. Martin, S. Hagen, F. Leyssner, S. Soubatch, J. Meyer, M. Wolf, P. Tegeder, F. S. Tautz, et al., Structure and Energetics of Azobenzene on Ag (111): Benchmarking Semiempirical Dispersion Correction Approaches, Physical review letters **104**, 036102

(2010).

[14] X. Fan, C.-H. Chang, W. Zheng, J.-L. Kuo, and D. J. Singh, The electronic properties of single-layer and multilayer MoS_2 under high pressure, The Journal of Physical Chemistry C **119**, 10189 (2015).

[15] A. Jain, S. P. Ong, G. Hautier, W. Chen, W. D. Richards, S. Dacek, S. Cholia, D. Gunter, D. Skinner, G. Ceder, et al., Commentary: The materials project: A materials genome approach to accelerating materials innovation, APL materials **1** (2013).

[16] T. H. Fischer and J. Almlof, General methods for geometry and wave function optimization, The Journal of Physical Chemistry **96**, 9768 (1992).

[17] A. Marini, C. Hogan, M. Grüning, and D. Varsano, Yambo: an ab initio tool for excited state calculations, Computer Physics Communications **180**, 1392 (2009).

[18] D. Sangalli, A. Ferretti, H. Miranda, C. Attaccalite, I. Marri, E. Cannuccia, P. Melo, M. Marsili, F. Paleari, A. Marrazzo, et al., Many-body perturbation theory calculations using the yambo code, Journal of Physics: Condensed Matter **31**, 325902 (2019).

[19] G. Onida, L. Reining, and A. Rubio, Electronic excitations: density-functional versus many-body Green's-function approaches, Reviews of modern physics **74**, 601 (2002).

[20] G. Strinati, Application of the green's functions method to the study of the optical properties of semiconductors, La Rivista del Nuovo Cimento (1978-1999) **11**, 1 (1988).

[21] M. Grüning and C. Attaccalite, Second harmonic generation in h-BN and MoS_2 monolayers: Role of electron-hole interaction, Physical Review B **89**, 081102 (2014).

[22] C. Attaccalite, A. Nguer, E. Cannuccia, and M. Grüning, Strong second harmonic generation in SiC, ZnO, GaN two-dimensional hexagonal crystals from first-principles many-body calculations, Physical Chemistry Chemical Physics **17**, 9533 (2015).

[23] W. Zhao, J. Pan, Y. Fang, X. Che, D. Wang, K. Bu, and F. Huang, Metastable MoS_2: crystal structure, electronic band structure, synthetic approach and intriguing physical properties, Chemistry–A European Journal **24**, 15942 (2018).

[24] T. Jiang, H. Liu, D. Huang, S. Zhang, Y. Li, X. Gong, Y.-R. Shen, W.-T. Liu, and S. Wu, Valley and band structure engineering of folded MoS_2 bilayers, Nature nanotechnology **9**, 825 (2014).

[25] A. A. Puretzky, L. Liang, X. Li, K. Xiao, K. Wang, M. Mahjouri-Samani, L. Basile, J. C. Idrobo, B. G. Sumpter, V. Meunier, et al., Low-frequency raman fingerprints of two-

dimensional metal dichalcogenide layer stacking configurations, ACS nano **9**, 6333 (2015).

[26] K. Ghatak, K. N. Kang, E.-H. Yang, and D. Datta, Controlled edge dependent stacking of WS_2-WS_2 Homo-and WS_2-WSe_2 Hetero-structures: A Computational Study, Scientific reports **10**, 1648 (2020).

[27] X. Li, X. Shi, D. Marian, D. Soriano, T. Cusati, G. Iannaccone, G. Fiori, Q. Guo, W. Zhao, and Y. Wu, Rhombohedral-stacked bilayer transition metal dichalcogenides for high-performance atomically thin CMOS devices, Science Advances **9**, eade5706 (2023).

[28] R. Dong, A. Jacob, S. Bourdais, and S. Sanvito, High-throughput bandstructure simulations of van der Waals hetero-bilayers formed by 1T and 2H monolayers, npj 2D Materials and Applications **5**, 26 (2021).

[29] M. Kan, J. Wang, X. Li, S. Zhang, Y. Li, Y. Kawazoe, Q. Sun, and P. Jena, Structures and phase transition of a MoS_2 monolayer, The Journal of Physical Chemistry C **118**, 1515 (2014).

[30] J. Van Baren, G. Ye, J.-A. Yan, Z. Ye, P. Rezaie, P. Yu, Z. Liu, R. He, and C. H. Lui, Stacking-dependent interlayer phonons in 3R and 2H MoS_2, 2D Materials **6**, 025022 (2019).

[31] G. Eda, T. Fujita, H. Yamaguchi, D. Voiry, M. Chen, and M. Chhowalla, Coherent atomic and electronic heterostructures of single-layer MoS_2, ACS nano **6**, 7311 (2012).

[32] L. F. Mattheiss, Band structures of transition-metal-dichalcogenide layer compounds, Physical Review B **8**, 3719 (1973).

[33] X.-L. Fan, Y. Yang, P. Xiao, and W.-M. Lau, Site-specific catalytic activity in exfoliated MoS_2 single-layer polytypes for hydrogen evolution: basal plane and edges, Journal of Materials Chemistry A **2**, 20545 (2014).

[34] X. Sun, Z. Wang, Z. Li, and Y. Q. Fu, Origin of structural transformation in mono-and bi-layered molybdenum disulfide, Scientific reports **6**, 26666 (2016).

[35] X. Qian, J. Liu, L. Fu, and J. Li, Quantum spin hall effect in two-dimensional transition metal dichalcogenides, Science **346**, 1344 (2014).

[36] K. F. Mak, C. Lee, J. Hone, J. Shan, and T. F. Heinz, Atomically thin MoS_2: a new direct-gap semiconductor, Physical review letters **105**, 136805 (2010).

[37] M. Mičica, S. Ayari, M. Hemmat, M. Arfaoui, D. Vala, K. Postava, H. Vergnet, J. Tignon, J. Mangeney, S. Guo, X. Yu, Q. J. Wang, Z. Liu, S. Jaziri, F. Carosella, R. Ferreira, and S. Dhillon, Determining Bandgaps in the Layered Group-10 2D Transition Metal Dichalcogenide $PtSe_2$, Advanced Functional Materials **n/a**, 2408982,

https://onlinelibrary.wiley.com/doi/pdf/10.1002/adfm.202408982.

[38] P.-C. Yeh, W. Jin, N. Zaki, D. Zhang, J. T. Liou, J. T. Sadowski, A. Al-Mahboob, J. I. Dadap, I. P. Herman, P. Sutter, et al., Layer-dependent electronic structure of an atomically heavy two-dimensional dichalcogenide, Physical Review B **91**, 041407 (2015).

[39] D. Voß, P. Krüger, A. Mazur, and J. Pollmann, Atomic and electronic structure of WSe_2 from ab initio theory: Bulk crystal and thin film systems, Physical Review B **60**, 14311 (1999).

[40] Z. Li, J. Förste, K. Watanabe, T. Taniguchi, B. Urbaszek, A. S. Baimuratov, I. C. Gerber, A. Högele, and I. Bilgin, Stacking-dependent exciton multiplicity in WSe_2 bilayers, Physical Review B **106**, 045411 (2022).

[41] N. T. Hung, A. R. Nugraha, and R. Saito, Two-dimensional MoS_2 electromechanical actuators, Journal of Physics D: Applied Physics **51**, 075306 (2018).

[42] G. Kourmoulakis, S. Psilodimitrakopoulos, G. M. Maragkakis, L. Mouchliadis, A. Michail, J. A. Christodoulides, M. Tripathi, A. B. Dalton, J. Parthenios, K. Papagelis, et al., Strain distribution in WS_2 monolayers detected through polarization-resolved second harmonic generation, Scientific Reports **14**, 15159 (2024).

[43] Z. Zeng, X. Sun, D. Zhang, W. Zheng, X. Fan, M. He, T. Xu, L. Sun, X. Wang, and A. Pan, Controlled vapor growth and nonlinear optical applications of large-area 3R phase WS_2 and WSe_2 atomic layers, Advanced Functional Materials **29**, 1806874 (2019).

[44] R. W. Boyd, A. L. Gaeta, and E. Giese, Nonlinear optics, in Springer Handbook of Atomic, Molecular, and Optical Physics (Springer, 2008) pp. 1097–1110.

[45] J. Shi, P. Yu, F. Liu, P. He, R. Wang, L. Qin, J. Zhou, X. Li, J. Zhou, X. Sui, et al., 3R MoS_2 with broken inversion symmetry: a promising ultrathin nonlinear optical device, Advanced Materials **29**, 1701486 (2017).

[46] E. Mishina, N. Sherstyuk, S. Lavrov, A. Sigov, A. Mitioglu, S. Anghel, and L. Kulyuk, Observation of two polytypes of MoS_2 ultrathin layers studied by second harmonic generation microscopy and photoluminescence, Applied Physics Letters **106** (2015).